Vanadium-Dioxide-Based Reconfigurable Ka-Band Dual-Sense Linear-to-Circular Polarizer

Mark S. Lust, *Student Member, IEEE*, David L. West, *Graduate Student Member, IEEE*,
Vanessa Smet, *Member, IEEE*, Thomas G. Williamson, *Member, IEEE*,
and Nima Ghalichechian, *Senior Member, IEEE*

Abstract— We propose a reconfigurable dual-sense linear-to-circular polarization (LCP) converter in the form of a VO$_2$-based metasurface. VO$_2$ is a phase change material (PCM) that is useful for low-loss mmWave devices, being transparent in its insulating state and metallic when heated. The device operates in the satellite communications uplink portion of Ka-band (27.5–31 GHz). It consists of a four-layer meanderline metasurface with two overlapping configurations, rotated relatively by 90° in-plane, for right-hand circular polarization (RHCP) and left-hand circular polarization (LHCP) conversion. Each configuration is interrupted by VO$_2$ patches with double spiral NiCr microheaters along the meandered traces. Under dc bias, the VO$_2$ of one trace changes from insulator to conductor, activating the configuration. The simulated design exhibits axial ratio (AR) $\leq$ 0.99 dB and insertion loss (IL) $\leq$ 2.59, for both RHCP and LHCP conversion. After verifying the dual-sense RF design in simulation, single-sense LCP conversion was measured. The measured results are for LHCP conversion with AR $\leq$ 2.1 dB and IL $\leq$ 4.0 dB. The LHCP conversion also has 1-dB AR from 30.2–32.4 GHz and 3-dB AR from 27–38 GHz (26% circular polarization bandwidth). This study demonstrates for the first time LCP conversion using a transmission-mode reconfigurable metasurface in Ka-band using VO$_2$ PCM, and simple dc activation network.

Index Terms— Linear-to-circular polarization (LCP), metasurface, mmWave, phase change material (PCM), reconfigurable, VO$_2$.

I. INTRODUCTION

AS COMMUNICATION networks become more and more crowded with the growing population of Internet-connected devices, new avenues of signal diversity are sought to alleviate interference. Notably, the available communication frequency bands are being expanded with the advent and

Mark S. Lust was with ElectroScience Laboratory, The Ohio State University, Columbus, OH 43212 USA. He is now with the Cyber Trust and Analytics Division, Battelle Memorial Institute, Columbus, OH 43212 USA (e-mail: Lust.50@osu.edu).

David L. West, Thomas G. Williamson, and Nima Ghalichechian are with the School of Electrical and Computer Engineering, Georgia Institute of Technology, Atlanta, GA 30308 USA (e-mail: dwest64@gatech.edu; thomas.williamson@gtri.gatech.edu; nima.1@gatech.edu).

Vanessa Smet is with the George W. Woodruff School of Mechanical Engineering, Georgia Institute of Technology, Atlanta, GA 30308 USA (e-mail: vanessa.smet@me.gatech.edu).
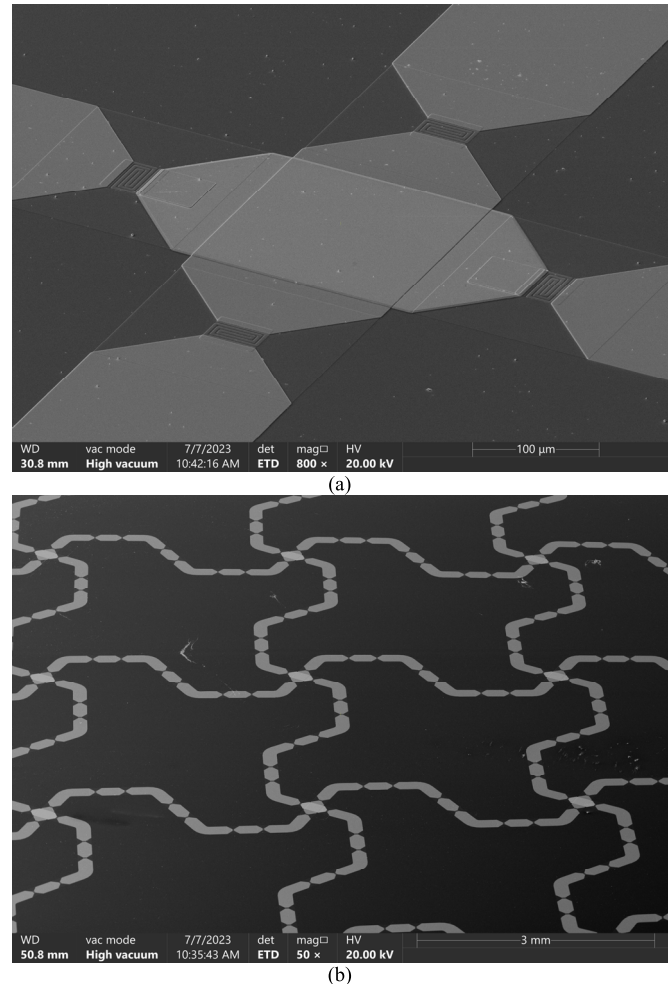
Fig. 1. Scanning electron microscope (SEM) micrographs of reconfigurable polarizer device (a) close-up of junction between configurations and (b) overview of several unit cells.

proliferation of 5G networks and the use of the Ka-band in satellite communications (satcom). These increase accessible bandwidth and number of active channels; however, there is opportunity for new dimensions of modulation and multiplexing in this paradigm. To improve robustness against signal interference and network interruptions, we can create diversity not only in the frequency domain but also in polarization.

Usage of circular polarization (CP) is desirable as opposed to linear polarization (LP), as it eliminates the risk of polarization mismatch loss due to misalignment [1]. This is especially useful in mobile networks, where handheld devices are positioned at any and every angle imaginable. Additionally, in satcom, where spacecraft are thousands or tens of thousands

of miles away, any reduction in pointing or aligning requirements is highly beneficial.

Current literature on linear to circular polarization (LCP) converters is focused on implementing dual-sense-dual-frequency LCP metasurfaces and antennas [1], [2], [3]. These provide static LCP conversion with each sense of CP assigned to its own frequency band. There are also switchable reflection-mode LCP conversion metasurfaces that produce either LP or CP with PIN-diodes [4] and varactor diodes [5], dual-sense reflection-and transmission-mode LCP converters with mechanical reconfiguration [6], liquid metal injection microfluidics [7], [8], liquid crystal [9], and transmission mode single-sense reconfigurable LCP converters using PIN-diodes [10], [11]. The creation of reconfigurable CP-sense diversity within a single band in a phase change material (PCM)-based transmission-mode metasurface is yet to be explored.

Having both right-handed circular polarization (RHCP) and left-handed circular polarization (LHCP) in the same space is attractive as they are orthogonal and will not destructively interfere with each other. A reconfigurable dual-sense LCP converter effectively doubles available bandwidth in the case that nearby networks cause interference, lowering signal strength (therefore, signal-to-noise ratio, SNR), and ultimately causing slow device connection. While the doubled bandwidth is not simultaneous per device, it allows several multi-in-multi-out (MIMO) networks to run smoothly in parallel. For example, a home 5G router with dual-sense reconfigurable LCP conversion could enhance its agility by dodging nearby interfering signals through switching polarization in addition to conventional channel hopping.

As applied to satcom, the dual-sense LCP conversion is advantageous in using a single aperture to communicate with various satellites that could have static RHCP or LHCP antennas. It is preferable to have any method of reconfiguration on the ground side, as static devices consume less power and can weigh less. Weight reduction in satellites dramatically reduces the cost of launching into space, as it directly impacts the amount of thrust required. Lowering power consumption allows the limited energy absorbed by onboard photovoltaics to be dedicated to scientific instrumentation and measurement or signal processing and computation.

In this work, we present the design, fabrication, and measurement of a reconfigurable dual-sense LCP converter metasurface based on vanadium dioxide (VO_2). VO_2 provides a path for achieving low-loss mmWave switches. PIN and varactor diodes are widely used in the microwave band; however, they suffer from large losses at the mmWave band. MEMS switches are difficult to fabricate and integrate on the electromagnetic metasurface and require large actuation voltage. In contrast, nonlinear behavior of VO_2 can be exploited to create low loss mmWave switches with millisecond response time. This response time is thermally limited; the phase transition mechanism has been shown to occur on a picosecond timescale for ultrafast laser pulses [12]. Scanning electron microscope (SEM) micrographs of a fabricated metasurface device are shown in Fig. 1. Measurement results for the metasurface device have previously been presented in recent conferences [13], [14].
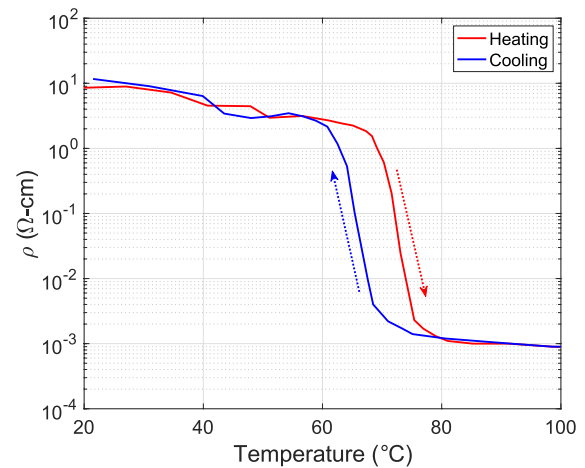

Fig. 2. VO_2 phase change shown as electrical resistivity over temperature as grown on annealed Al_2O_3 [32].

A. VO_2 PCM

Phase change materials or PCMs are used in reconfigurable and "smart" devices, be it sensors [15], [16], [17], [18], antennas [19], [20], switches [21], [22], [23], [24], [25], [26], metasurfaces [27], [28], or power limiters [29], [30], [31]. The advantages of PCMs over typical solid-state switches include quasipassive behavior; the range of options of external stimuli such as Joule heating, voltage, current, strain, infrared light, or X-rays, and direct manipulation of device geometry. VO_2 is a PCM with a reversible insulator–metal transition (IMT) at 68 °C, with contrast in electrical resistivity of 9.8×10^4 when grown on C-plane sapphire and 1.46×10^4 when grown on Si with an annealed Al_2O_3 buffer layer [32]. During the IMT, the crystal structure of the VO_2 switches from monoclinic to tetragonal, and back again when cooled. This change is illustrated in Fig. 2 [32]. VO_2 is especially appealing in mmWave systems for its low material losses compared to solid-state semiconductor switches. It is also highly reliable for mmWave applications, as experimentally demonstrated in our prior work, with no significant degradation after 100 million thermal cycles. Additionally, the actuation was done using a 100 Hz 10% duty cycle wave (1-ms pulses) when using Joule heaters [33]. While it is frequently deposited on sapphire substrates with the highest resistivity contrast, it is generally of better interest in mmWave systems to integrate VO_2 on Si substrates. The advantages provided by using Si substrates are the ability to perform bulk micromachining to locally modify metasurface substrate thickness and potential for future packaged systems with control circuitry integrated monolithically with the metasurface. We note that while VO_2 exhibits low losses and high contrast ratio at the mmWave band, it can also be used as a tunable medium at other bands such as medium infrared as shown by our prior work [34].

B. Reconfigurable LCP Converter Concept

For our device, we chose to pursue dual-sense LCP conversion with a single aperture over the same band. We chose the Ka-band, specifically the satcom uplink frequencies of 27.5–31 GHz, because it also contains the 28 GHz 5G
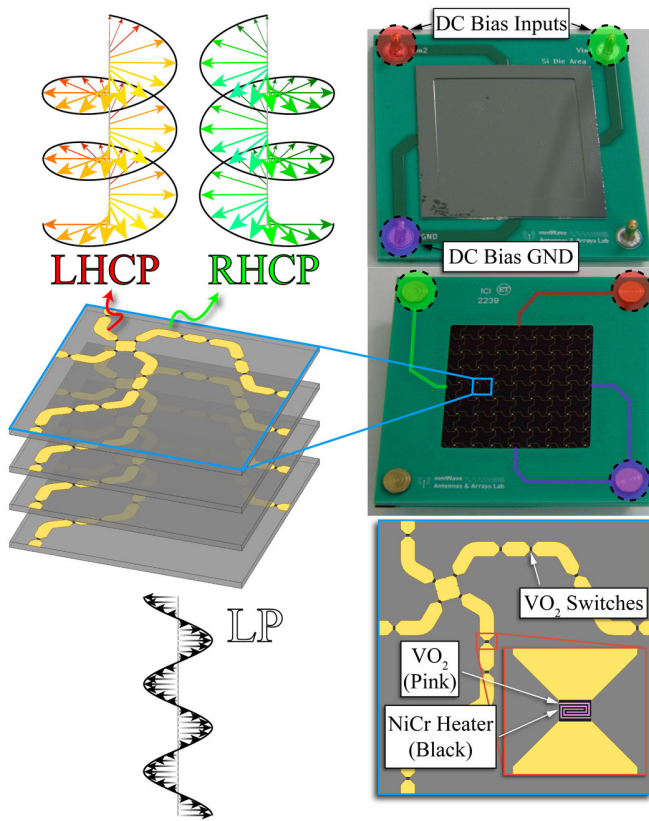
Fig. 3. Reconfigurable Ka-band polarizer operation. Each configuration is excited by a single dc voltage that separately produces LHCP or RHCP. The images in the top right are both sides of the fabricated and assembled device, and on the left is the model of the unit cell simulated in HFSS. The bottom right shows a top-down view of the unit cell.

range. The design principle for this device is based on the meanderline polarizer [35] with multiple cascaded layers [3], [36]. Original to our design is the addition of breaks in the meanderline traces connected with VO$_2$ PCM switches. The full design is duplicated and rotated 90° about the intersection point as first reported in our preliminary work in [37]. The device operation is illustrated in Fig. 3. The goal is to construct two superimposed meanderline polarizers that are isolated in dc and each transparent when the other is activated. To enable the overlapping design, we applied the concept of the meanderline trace to a hexagonal grid so that there is less interaction between the two configurations. The shift from rectangular to hexagonal meanderlines is depicted in Fig. 4. The motivation behind having the hexagonal overlaid meanderlines was twofold: to have identical behavior between the two configurations and to maximize unit cell dimensions. A rectangular shape like the one shown in Fig. 4(a) would overlap at multiple points with 90° overlaid configurations. Square proportions for a rectangular grid meanderline would serve the device's function, but the hexagonal grid allows decreased mutual coupling between the ON and OFF configurations. Another aspect to consider was unit cell size. This is discussed in further detail in Section II-A. The decision for using the hexagonal grid over rectangular was influenced by engineering considerations, taking advantage of the fact that the underlying

physics principles of the hexagonal grid and rectangular grid meanderlines are the same, discussed below.

The operating principle of the meanderline polarizer begins with a diagonal 45° LP wave excitation. This wave is broken down into vertical and horizontal components, which encounter shunt inductance along the traces and shunt capacitance across the traces, respectively. The layout causes a 90° difference ($\Delta\varphi$) in phase between the two components that then reunite as a CP wave [35]. In our case, the vertical and horizontal components stay the same, but when the alternate configuration is active, the vertical component encounters shunt capacitance across the traces, and the horizontal component interacts with shunt inductance along the traces. In the alternate configuration, $\Delta\varphi = -90°$ (1). Equations for amplitude error, A_e, and phase error, φ_e, are given in (2) and (3). Amplitude error is the difference between the transmission coefficients of the vertical and horizontal modes. The phase error is the deviation in phase difference from 90°. The simple input switching scheme is enabled by using VO$_2$. The novelty of the approach lies in the rotational-symmetric dual configuration and the VO$_2$ PCM-based switching scheme.

$$\Delta\varphi = \varphi_V - \varphi_H \tag{1}$$
$$A_e = 20\log_{10}\big(1 + \big|S_{21,V} - S_{21,H}\big|\big) \tag{2}$$
$$\varphi_e = 90 - |\Delta\varphi|. \tag{3}$$

II. DESIGN AND SIMULATION

A. Electromagnetic Design

Modeling and simulation of the electromagnetic (EM) design was carried out using ANSYS HFSS. We performed simulations using Floquet ports and periodic boundaries for an infinite array. The unit cell, shown in Fig. 5, consists of a 100 μm thick Si substrate, 500 nm thick Ag meanderline traces, 100 nm thick VO$_2$ at Ag gaps, and 150 nm thick NiCr double spiral heaters on top of the VO$_2$; these are repeated as four layers, 600 μm apart from the top of one layer to the top of the next. The vertical and horizontal traces are based on a hexagonal grid with 1.1 mm long segments such that they only intersect at one point and are identical save for the 90° rotation about their intersection point. With the need for rotational symmetry, the traces are somewhat sparse and cannot create 90° phase difference with one layer. Therefore, the initial design was made for one layer that causes ~22.5° phase shift, then increased to four layers, where the pitch between the layers and the Si thickness were optimized for the 90° phase difference target. The VO$_2$ patches along the vertical traces are assigned with the properties of its metallic state, and the VO$_2$ patches along the horizontal traces are assigned the properties of its dielectric state.

In each unit cell, there are 8 VO$_2$ switches per configuration. The number of switches was chosen based on the interplay between several factors: losses, power consumption, and resonant behavior. With too many switches, conductivity of the ON-configuration becomes too low, causing higher losses, and the power consumption increases proportionally. With too few switches, power consumption is lower. However, the solid sections of the main conductor become too large and cause
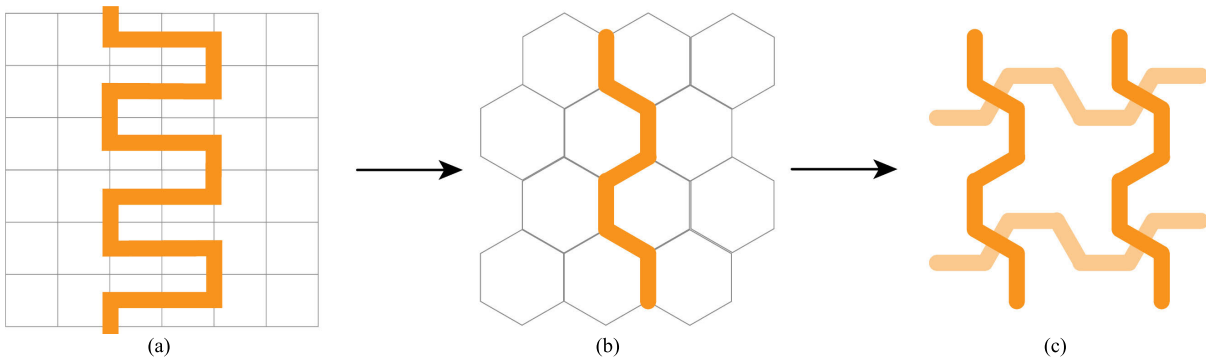
Fig. 4. Evolution of our design from (a) traditional meanderline, to (b) hexagonal grid meanderline, and to (c) rotated and overlaid hexagonal grid meanderlines.
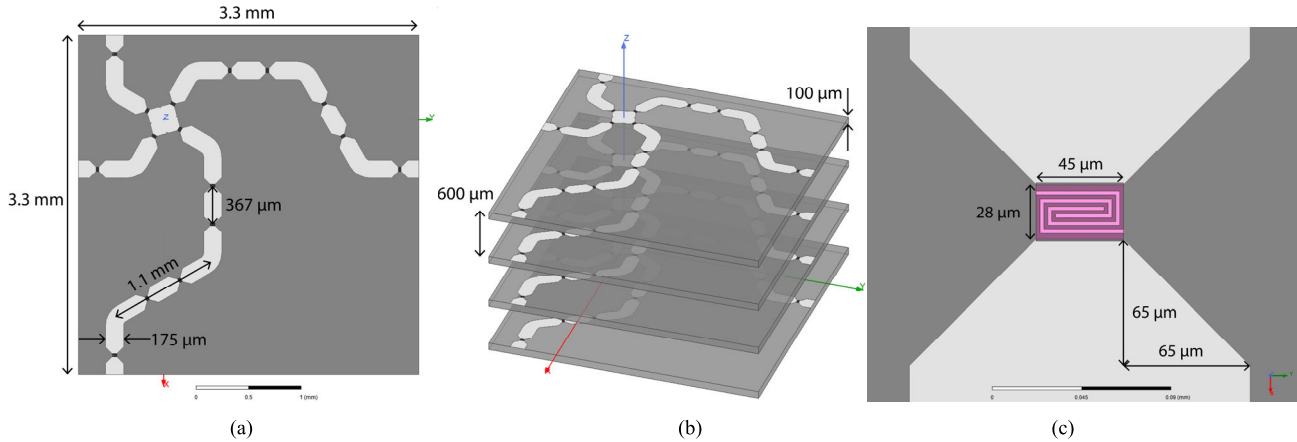

Fig. 5. HFSS model (a) top view of unit cell with dimensions, (b) trimetric view of unit cell showing four layers with dimensions, and (c) top view close-up of VO_2 switch with NiCr heater and dimensions. NiCr heater and gap are each 2 μm wide.
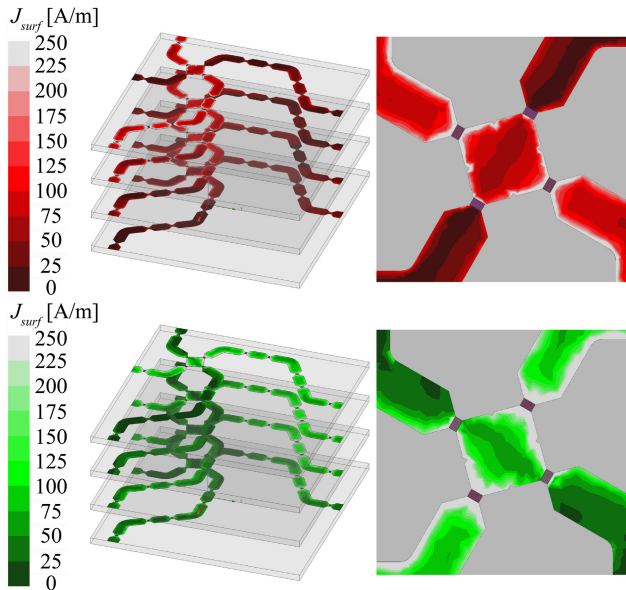

Fig. 6. RF surface current distribution in the metasurface with (top) LHCP mode active and (bottom) RHCP mode active presented (left) over the full unit cell and (right) at the junction between the traces.

The implementation of a hexagonal grid accomplishes two goals: lower coupling between configurations and larger unit cell size. The hexagonal grid allows sparser layout than square, so potential field coupling to the neighboring traces is lower. Compared to a rectangular grid meanderline, the unit cell has a 50% increase in side length to 3.3 mm, or $\lambda/3$ at 30 GHz. The larger unit cell allows for fewer total unit cells and therefore fewer total heaters and lower power consumption for the same overall device area. The full device was made as large as possible while having all four layers fabricated on a single 100-mm wafer, discussed in Section III. Therefore, it was critical to minimize power requirements per device unit area.

The switches consist of a rectangular patch of VO_2 with the double spiral NiCr heaters, set in the gaps with a chamfer design in the main meanderline traces. The chamfer detail was added to reduce continuity in the OFF state caused by capacitance in the gap. This allowed further isolation between the RF configurations. The size of the VO_2 patches was determined iteratively in a trade-off between smaller size to decrease resistance in the activated trace and larger to increase the gap and isolation in the deactivated trace. The VO_2 material boundary was limited to the NiCr heater area, as the intended active area of the switch.

The heaters were designed as double spirals to add an inductive RF choke function to the OFF state of the switches, giving greater EM isolation than a capacitive gap. Once the heater excites the VO_2, the turns of the double spirals are shorted together, causing the switch to act as a simple resistor.

the OFF-configuration to interact with the incoming wave and affect the performance of the ON-configuration. With four heaters, the main conductor sections would resonate in the OFF state within the operating band.
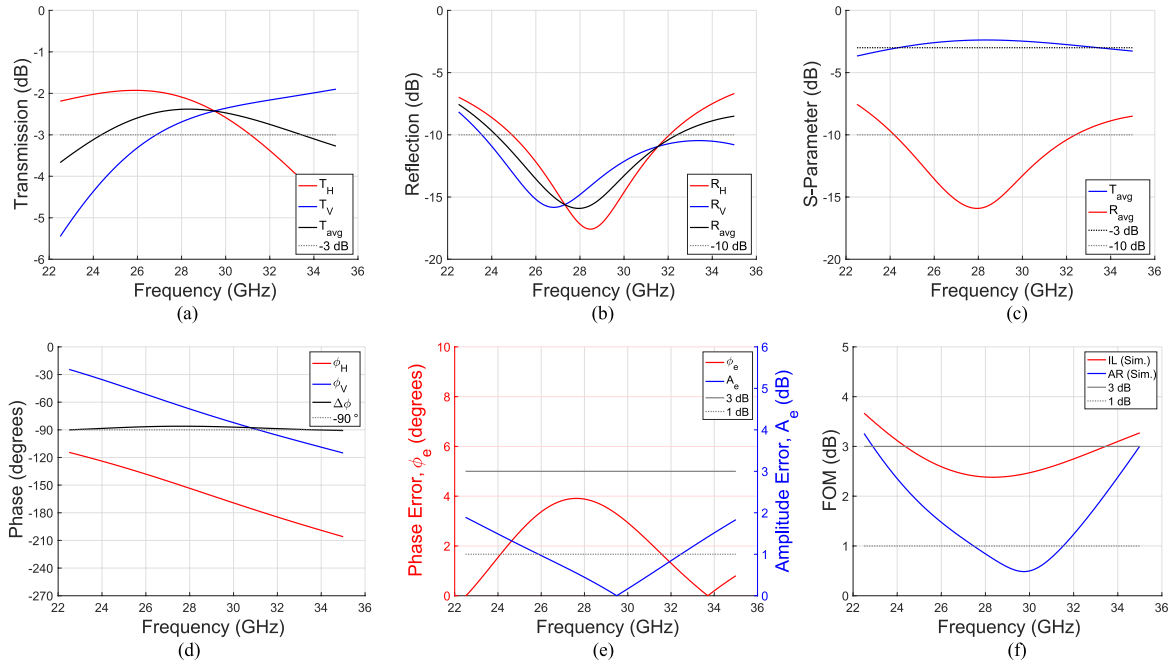
Fig. 7.   Simulation results for unit cell design (a)–(c) transmission and reflection, (d) phase accumulated in each Floquet mode and difference thereof, (e) phase and amplitude error, and (f) FOM: insertion loss and axial ratio.

TABLE I
RIE AND RIE-ICP RECIPES FOR VO$_2$ AND ALUMINA

Material Etched	RIE Power (W)	ICP Power (W)	Process Pressure (mTorr)	Ar flow (sccm)	SF$_6$ flow (sccm)	BCl$_3$ flow (sccm)
VO$_2$	100	0	5	20	20	0
Al$_2$O$_3$	50	400	10	10	0	30

The difference in RF surface current flow between the switch states is shown in Fig. 6, with clear disruption by the double spirals and continuity over the activated VO$_2$.

The Floquet ports are excited with two modes, defined in HFSS as TE$_{00}$ and TM$_{00}$, which are plane waves with 90° rotation between the two. The port excitations are deembedded to the top surface of the top layer and the bottom surface of the bottom layer. The reflection (S$_{11}$), transmission (S$_{21}$), and phase shift are compared between the vertical and horizontal modes. To find the difference in phase shift between the two modes (hereafter referred to as the phase difference), the absolute value is taken of the difference between the respective unwrapped phase shifts. Low reflection is a good benchmark, but the chief figures of merit (FOM) of the polarizer, namely the insertion loss (IL) and axial ratio (AR), are determined from the comparative and total S$_{21}$ and phase difference ($\Delta\varphi$). IL and AR are found in (4)–(6), respectively. Subscripts V and H refer to the vertical and horizontal wave components. Phase is calculated in degrees

$$IL = -20\log_{10}\left(\frac{S_{21,V} + S_{21,H}}{2}\right) \tag{4}$$

$$\Delta = \sqrt{1 - \frac{4S_{21,V}^2 S_{21,H}^2 (\sin\Delta\varphi)^2}{S_{21,V}^2 + S_{21,H}^2}} \tag{5}$$

$$AR = 20\log_{10}\sqrt{\frac{1+\Delta}{1-\Delta}}. \tag{6}$$

The simulated FOM results are AR $\leq$ 0.99 dB and IL $\leq$ 2.59 dB throughout the 27.5–31 GHz band. AR must be at most 3 dB to be considered circular polarization, so less than 1 dB is an excellent result. IL is typically considered in a 1-dB bandwidth for static LCP converters [1], [2], [3], but reconfigurability comes with a trade-off of larger losses [38]. This trade-off of higher losses considered, we decided to compensate with a stricter AR design goal of 1 dB. Lower AR implies a lower range for potential polarization mismatch loss. Given the unit cell's rotational symmetry, the alternate configuration results are identical, only with swapped transmittance and reflectance profiles per mode and negative phase difference.

The reflection and transmission are shown for the two modes and the average in Fig. 7(a)–(c); phase shift, phase error, and amplitude error are illustrated in Fig. 7(d) and (e); and FOM results are plotted in Fig. 7(f). The cross-polarized reflection and transmission of the plane wave modes were found to be below −40 dB across the band, indicating strong isolation between the orthogonal modes.

B. Thermo-Electric Switch Design

The switch design was largely based on the EM model. The trace width and height and double-spiral design were chosen for their effect on the EM performance. The resulting resistance of a single heater at room temperature was 1 kΩ. Due to inherent difficulties in simulating the sharp, nonlinear switching behavior of VO$_2$ with Joule heating combined with voltage and current effects, we chose to experimentally verify the dc portion of its functionality. We fabricated and tested several experimental standalone dc switch devices on a probe station before processing the full metasurface. These included single switches and sets of switches in series.

When measured on a dc probe station, the switches were confirmed to activate with a combination of Joule heating
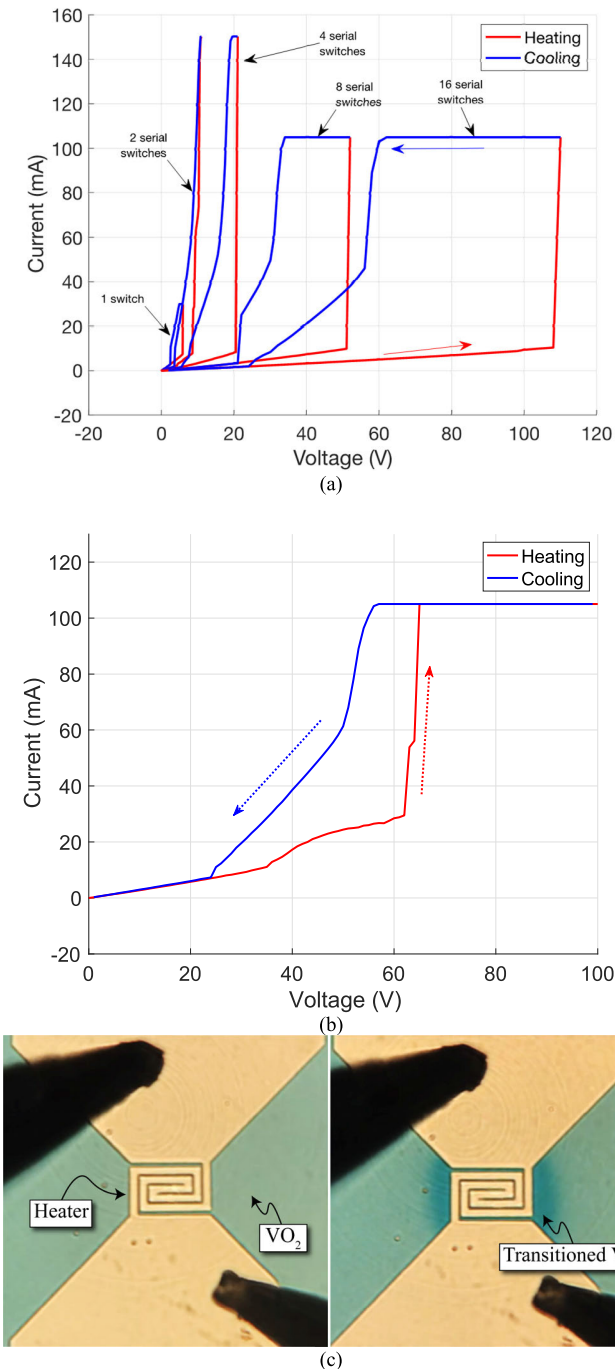
(a)

(b)

(c)

Fig. 8. Dc probe station measurements of test switches. I–V plots of (a) various sets of test switches in series and (b) one layer of the metasurface device. (c) Micrographs showing a single test switch in the OFF state (left) and in the ON state (right), where an isolated section of VO$_2$ is transitioned, as indicated by the color change.

Fig. 9. Process flow for polarizer device. Starting with RIE patterning of VO$_2$, NiCr was then evaporated and lifted off, followed by evaporation and lift-off of Au, then ALD alumina. The alumina was then etched using RIE-ICP, and the final Au layer was deposited. Last, the back side was etched by 200 μm using DRIE.

from the NiCr and field effect from the applied voltage. The Joule heating reduces the voltage required to activate VO$_2$. Detailed switching behavior for a single switch, different sets of serial switches, and a full layer of the metasurface are depicted in Fig. 8 alongside a pair of micrographs of a test switch. Measurements were taken using a Keithley source meter. In the full metasurface layer, we observed that the VO$_2$ begins to transition at 35 V, then fully transitions as it hits the tool's compliance limit of 105 mA after the sharp transition 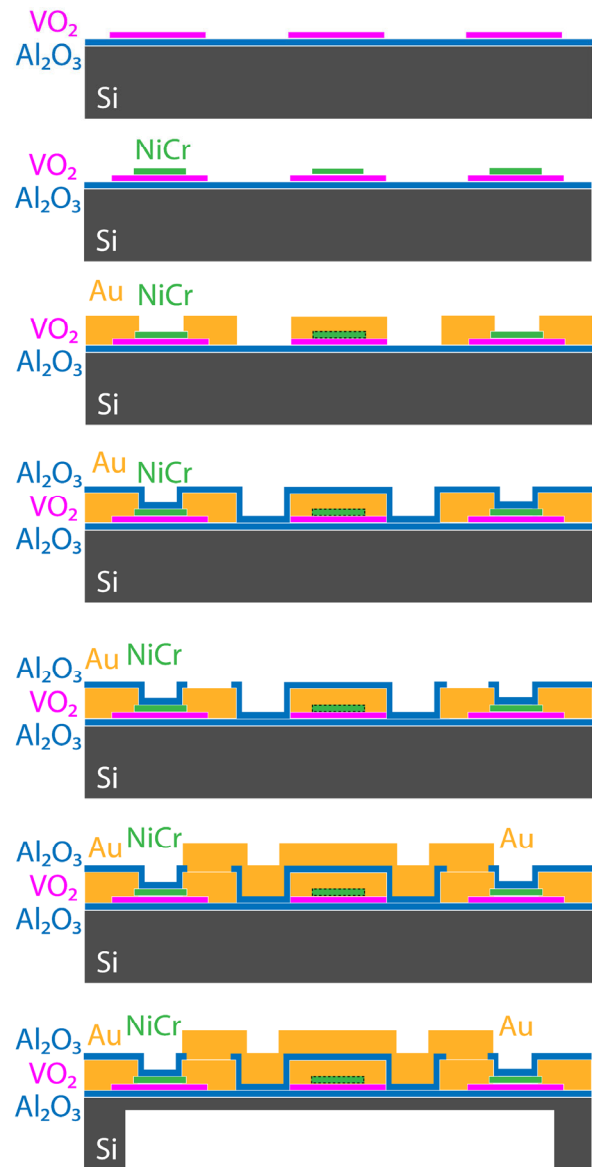from 63 to 65 V. When cooling, the current remains maxed out until it reduces to 57 V, then it begins to drop, showing a total resistance around 90 Ω, increasing around 50 V to 500 Ω. Note that the transition voltage is lower in the full metasurface layer, as it consists of eight parallel sets of 64 serial resistors. As such, it is reasonable to see this slightly different behavior from the sets of test switches. As the metasurface layers are all in parallel, this is representative of the expected voltage required for testing and 1/4 the current. Flat areas of the curves show where the source meter was at its hardware current limit for the given voltage. As shown in Fig. 8(c), when the switch is in the ON state (right), the transitioned VO$_2$ (indicated by the darker blue color) is well-confined to the heater area. The dc bias circuit within the metasurface uses the same traces as the RF circuit; this is inherent in the meanderline design
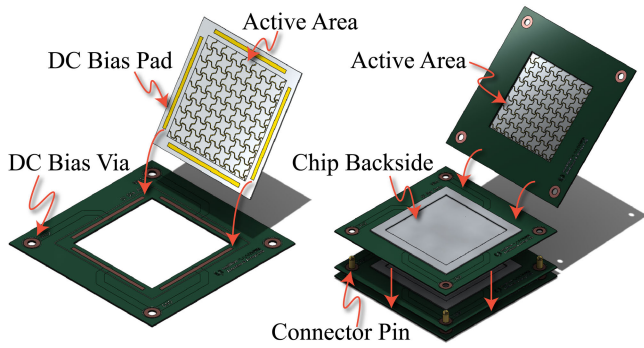
Fig. 10. Assembly procedure of the polarizer. We bond each metasurface chip to a PCB, and we layer four PCBs to complete assembly of the device. Connector pins ensure alignment between the layers and provide external dc connection points.
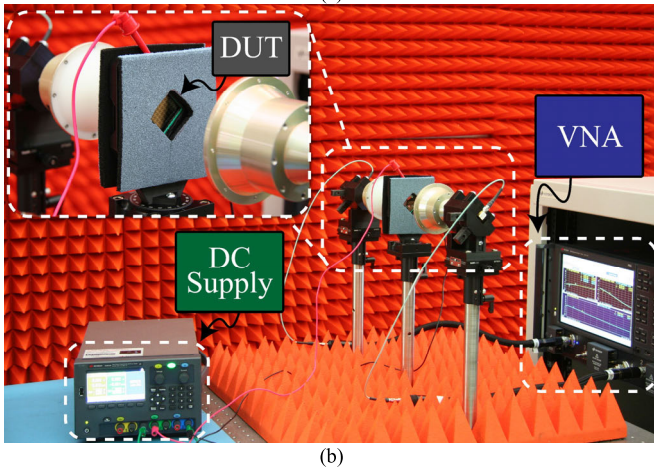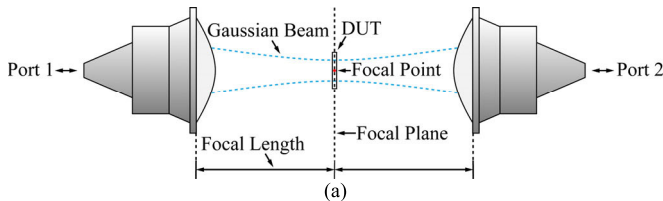

Fig. 11. (a) Schematic and (b) image of the quasioptical test setup. Lensed horn antennas focus a Gaussian beam onto the metasurface, which is placed at the focal point. The antennas are driven by a VNA, and a dc supply is used to bias the metasurface.

incorporating PCM. The two circuits work together for the simplest possible device activation.

III. DEVICE FABRICATION

A. Wafer-Level Processing

The fabrication process flow is shown in Fig. 9. Starting with a 300 μm thick 100 mm diameter high-resistivity float-zone (FZ) Si wafer, we deposited and annealed ALD alumina and sputtered VO_2 as described in our previous work [32]. This process enables deposition of a VO_2 film with a high contrast ratio on Si, which was previously only available for sapphire substrates. We then patterned and etched the VO_2 with the RIE process detailed in Table I. Next, we performed e-beam evaporation and lift-off of 150 nm thick 80/20 NiCr alloy, followed by e-beam evaporation and lift-off of 500 nm thick Au with a 5 nm thick seed layer and a 25 nm thick
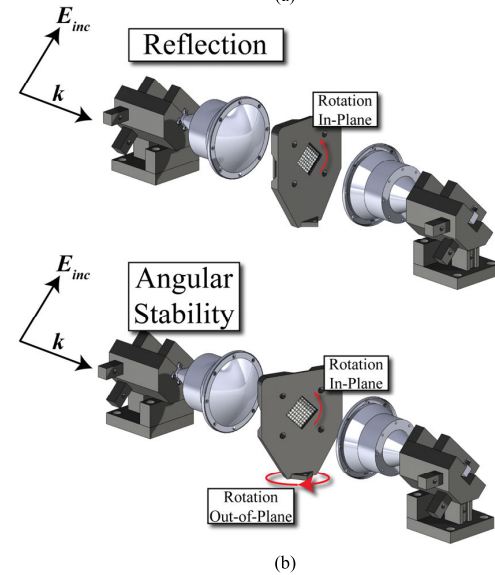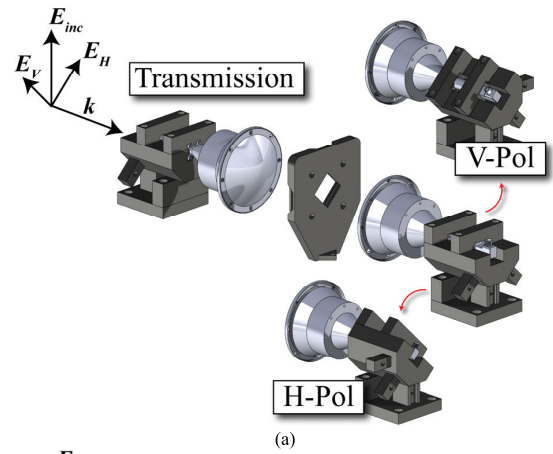

Fig. 12. Quasioptical measurement procedure. (a) Excitation of the metasurface with a diagonally polarized wave. We calibrated the system with both antennas in the vertical position and captured the V and H components of the circularly polarized output wave by rotating the receiving horn. (b) Independent measurement of the linearly polarized components to capture the reflection characteristic and angular stability. The DUT is rotated in-plane to capture each component. The DUT fixture is rotated out-of-plane to capture the response at different incident angles.

cap layer; for each of these, we used AZ nLOF 2020 negative photoresist with 2 μm thickness. The first layer of Au connected the horizontal traces end-to-end. To connect the vertical traces, we deposited a 200 nm alumina isolation layer and etched it using the RIE-ICP recipe detailed in Table I. Then, we performed e-beam evaporation and lift-off of a 500 nm Au layer, this time using AZ nLOF 2070, a thicker photoresist at 7 μm. Whereas the original ideal simulation used Ag as the main conductive material, we opted for Au after Ag-based prototypes exhibited dc shorts.

The full device unit cell substrate was 100 μm thick, so the next step was to use deep reactive ion etching (DRIE), also known as Bosch process, to etch 200 μm into the back of the substrate. First, we spin coated a film of S1813 photoresist and hard baked it to protect the front-side device layers. Afterward, we flipped the wafer and coated the back using AZ nLOF 2070 and patterned it having used the backside alignment feature of the maskless aligner (Heidelberg MLA150). We used 369 cycles of the following process: 5 s deposition using
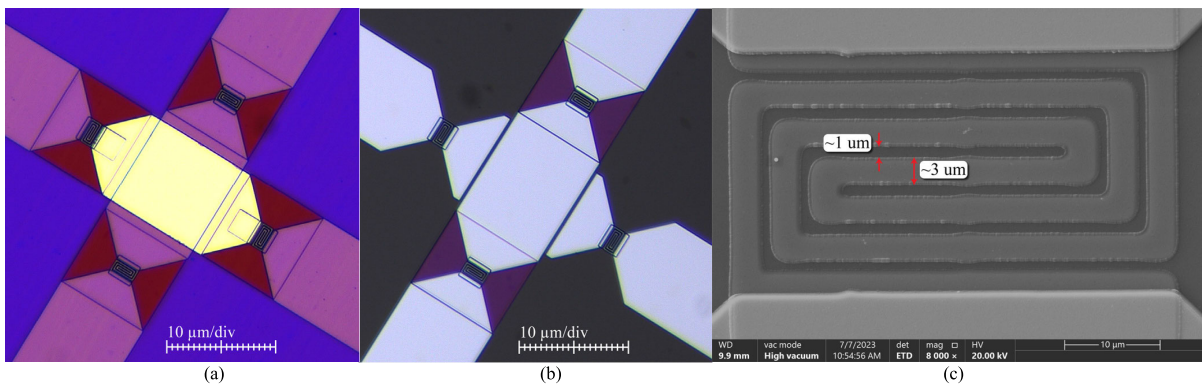
Fig. 13. Micrographs of the completed metasurface, (a) original version with two contiguous dc activation circuits, (b) ON/OFF version with both RF configurations present and one contiguous dc activation circuit and one interrupted dc circuit (i.e., with bridges and VO₂ excluded), and (c) SEM micrograph of NiCr heater dimensions changed due to undercutting in evaporation/lift-off.
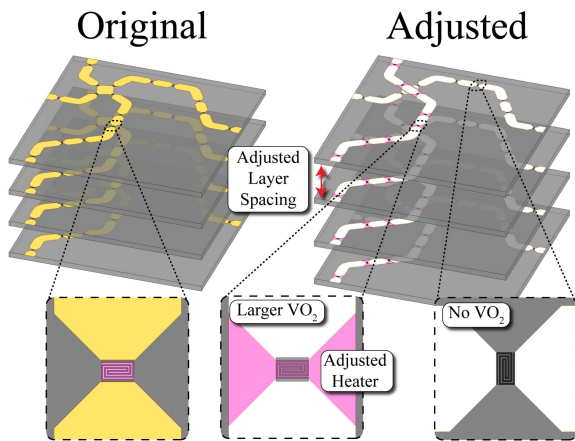

Fig. 14. Overview of the adjustments to the simulation model based on variables introduced in processing.

70 sccm C_4F_8, 1 sccm SF_6, 40 sccm Ar, 1 W RIE power, and 825 W ICP power at 15 mTorr; and 10 s etch using 5 sccm C_4F_8, 100 sccm SF_6, 40 sccm Ar, 9 W RIE power, and 825 W ICP power at 15 mTorr. To keep the substrate from overheating and burning the photoresist, 5-min rest periods were inserted every 50 cycles, and the wafer was stacked on a 100 mm Al_2O_3 wafer, 500 μm thick, to improve the seal on the chuck. The latter enhances the He cooling by increasing back pressure. We removed the photoresist using heated (80 °C) NMP (1-methyl-2-pyrrolidone). SEM micrographs of the finished device are shown in Fig. 1.

B. PCB Design and Assembly

To provide mechanical structure and accessible dc biasing, we used a packaging scheme with printed circuit boards (PCBs). The assembly is shown in Fig. 10. We bonded each metasurface chip to a PCB layer, and four assembled layers form the complete device. Because the metasurface was designed with the silicon layers separated by air gaps, we cut an aperture into the center of the PCB to expose the active area. Large dc pads provide the electrical connection between the PCB and the chip. The pads connect to plated vias in the corners, which form the dc input ports.

The PCB thickness is required to be 300 μm to achieve the desired layer pitch, and thicker copper is preferred to support

higher dc currents. To achieve these characteristics, four PCBs per full device are fabricated using Rogers RO4003 with a thickness of 8 mil (203 μm) and 2-oz copper cladding. After plating the vias, the final copper thickness is 3 oz (105 μm). We etch the backside copper on the PCB such that the chips are separated by one copper layer and one dielectric layer with a total thickness of 308 μm.

We chose silver epoxy (MG chemicals 9410-3ML) as the bonding material, as the low thickness of the chip-side metal precluded soldering. We used a pneumatic benchtop manual dispenser to deposit a controlled volume of silver epoxy onto the PCB landing pads, then we picked-and-placed each metasurface chip onto a PCB using a Finetech FINEPLACER Matrix flip-chip bonder with a placement accuracy of ±3 μm. We then cured the samples at 150 °C for 7 min on a hot plate. To complete assembly, four samples were layered and aligned using connector pins, which were soldered by hand.

A limited amount of force had to be used when placing the metasurface chips due to the risk of shorting connections if the silver epoxy is overcompressed. As such, the silver epoxy's final thickness increases the layer spacings by 120–230 μm (0.012–0.023λ at 30 GHz). We measured the layer spacings by viewing the final devices from the side using a microscope.

IV. QUASI-OPTICAL MEASUREMENT SETUP

We employed a quasioptical free space measurement setup to characterize the metasurface device. A diagram and an image of the test setup are shown in Fig. 11. We used a pair of Ka-band spot-focusing lensed horn antennas (Eravant SAQ-333039-28-S1). Measurement analysis begins at 27 GHz due to uncertainties near the cutoff frequency. The dielectric lenses focus the fields into a Gaussian beam with a focal length of 100 mm. The antennas are positioned two focal lengths apart with the DUT placed at the focal point, where there is a concentrated field intensity and planar phase front. The field intensity is characterized by the 3-dB beamwaist diameter, which is 12.7 mm in the E-plane. The setup emulates a plane wave incident on an infinite periodic structure, allowing for direct comparison with the Floquet port simulations. We used a PNA to perform the RF measurements, and we used a dc power supply to activate the metasurface. We applied
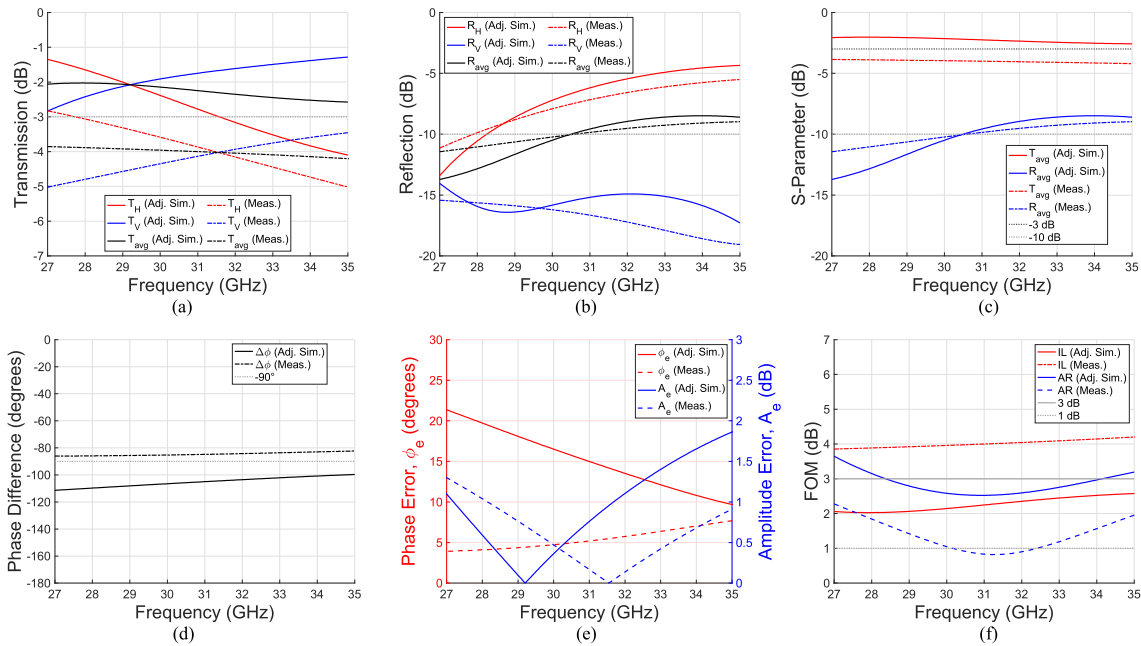
Fig. 15.   Measurement results with comparisons to simulations (a)–(c) transmission and reflection, (d) phase difference between the Floquet modes, (e) phase and amplitude error, and (f) FOM: insertion loss and axial ratio.
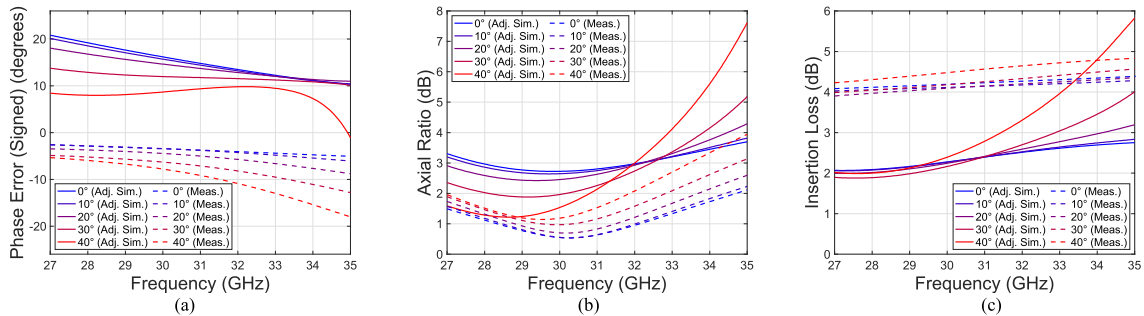

Fig. 16.   Measured angular stability results with comparison to the adjusted simulation. (a) Signed phase error, (b) axial ratio, and (c) insertion loss data for incident angles ranging from 0° to 40°.

50 V dc with a current limit of 350 mA to activate the DUT. The initial current draw was 30 mA and ramped up to 50 mA as the VO$_2$ approached the transition temperature. When the VO$_2$ transitioned, the current quickly increased to the 350-mA limit with a corresponding drop in the voltage. Peak power draw was briefly 17.5 W during the transition. For four layers, 64 unit cells per layer, and eight switches per unit cell, this corresponds to a peak power of 68.4 mW per unit cell, or 8.5 mW per switch. Upon activation, the current required to sustain LCP conversion dropped to 130 mA at 50 V, corresponding to a total running power of 6.5 W, with 24.4 mW per unit cell and 3.2 mW per switch.

Each chip is a square with a side length of 33.0 mm, and the active metasurface area has a side length of 26.4 mm. Fabrication limitations prevented ideal oversizing of the metasurface relative to the Gaussian beamwaist. Ideally, the sample size would be at least four times the 3-dB beamwaist, such that the beam is truncated where the fields are >35 dB below peak [39]. In this case, the ideal sample size is 50.8 mm or larger. To mitigate beam truncation effects, as shown in Fig. 11, we placed absorber on the DUT fixture around the edges of the aperture, and the fixture was left in place during calibration.

For flexibility in the measurement setup, the test lensed horn antennas were supported by 3-D-printed fixtures with stems that allowed them to be rotated in 45° increments. The DUT was also positioned at a 45° angle in its 3-D-printed fixture. As a result, the device may be tested by creating circular polarization with a diagonally polarized incident wave, and the two components of the circularly polarized output wave may be captured by rotating the receiving horn antenna. Alternatively, both horn antennas may be placed with the same polarization to individually capture the vertical and horizontal components to synthesize circular polarization as in the simulation. To facilitate angular stability measurements, the DUT was mounted on a rotating stage. The antennas were mounted on linear translation stages for positional adjustments along the axis of propagation. To minimize reflections from the optical table, the entire setup was raised using posts. Additional absorbers were placed on the table surface below the DUT.

We used a free-space thru-reflect-line (TRL) calibration. The *thru* standard included the empty DUT fixture with the antennas placed two focal lengths apart. The *reflect* standard was a small copper plate inserted in the DUT fixture. The *line* standard comprised the empty fixture with the antennas moved

apart by $\lambda/4$ at 30 GHz (2.5 mm) using the translation stages. We used time gating to eliminate undesired multipath effects due to repeated reflections between the antennas and DUT.

The procedure for transmission measurements at normal incidence is summarized in Fig. 12(a). We first calibrated the antennas in the vertical position. One antenna was then rotated at $\pm 45°$ to obtain the components of the circularly polarized output wave. The data were normalized to a thru measurement taken with the rotated receiving antenna. The normalization eliminates phase error incurred from misalignment of the antennas due to 3-D printing tolerances. In addition, the 3 dB of loss that would be expected from rotating the polarization of the receiving antenna is eliminated. As such, the normalized result can be compared to the unit cell simulations.

Reflection data for each component and measurements of angular stability required a separate procedure, shown in Fig. 12(b). We placed both horns at the $+45°$ position with their polarizations aligned and recalibrated. In this manner, the horizontal and vertical components are captured separately. We rotated the DUT by 90° in-plane to capture both components.

To capture the angular stability, we took transmission measurements at different incident angles by rotating the DUT stage using the same calibration. Only transmission results can be measured because specular reflection at off-normal incidence cannot be captured with the measurement setup. In addition, there is blockage of the beam due to the DUT fixture, which affects the transmission, so the measurement results have been normalized to thru measurements for the corresponding rotation angle. A maximum incident angle of 40° could be measured before the transmission is drastically affected.

V. MEASUREMENT RESULTS

We fabricated multiple versions of the metasurface. The versions of the device described in Section III were found to have thermal isolation issues between the VO_2 switches of the different configurations. Specifically, without the heat sink of the probe station present, the heat was no longer isolated to the area of the NiCr heaters. While we saw clear heat isolation to the switches on the probe station as shown in Fig. 8(c), the temperature distribution of the metasurface in final testing was uniform. As such, we present measurement results for an alternate version of the device, as shown in Figs. 13 and 14. VO_2 is only present for one set of meanderlines, and the bridges are not included. Additionally, the main conductor traces are Ag. To retain the effect of the OFF configuration on RF performance, the gaps in the Ag are narrow, and the NiCr heaters remain in place. This version is such that the presence of both RF configurations is represented, with one dc activation kept OFF to emulate thermal isolation. At room temperature, VO_2 is virtually transparent to mmWave radiation, so its selective absence is representative of its deactivated state. This device achieves one sense of circular polarization, which is activated when the VO_2 is heated. Along with the rotational symmetry, the concept is thus proven for the dual-sense LCP device in satisfaction of the mmWave design and implementation. The one remaining obstacle to dual-sense demonstration is improved thermal isolation between modes.
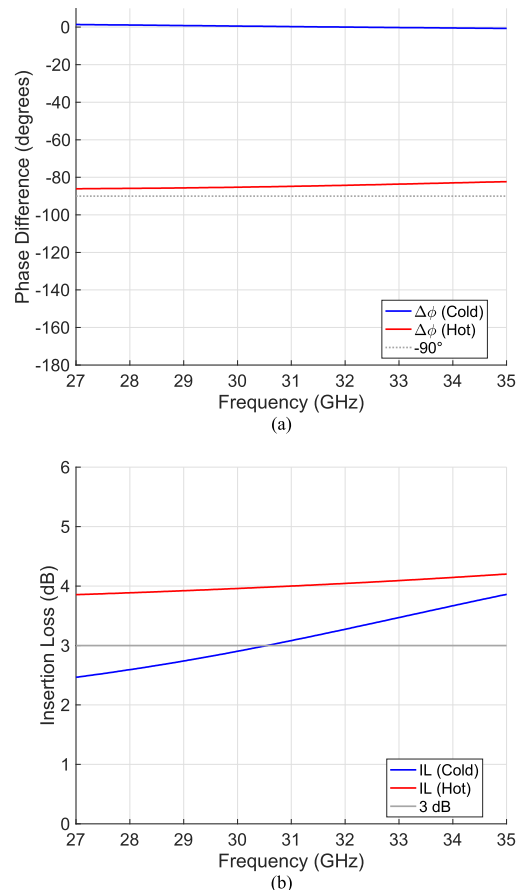

Fig. 17. Measurement results showing ON/Hot (LHCP) vs OFF/Cold (LP) performance in terms of (a) phase difference, and (b) insertion loss, demonstrating device reconfigurability.

Further iterations of thermal design are outside the scope of this project. The VO_2 area is larger in the fabricated devices compared to the original simulation, which ensures good ohmic contact between the meanderline trace and the VO_2 as well as eliminating alignment concerns. We also note that undercutting during the lift-off process for the heaters caused widening of the NiCr traces, as shown in Fig. 13.

In Fig. 15(a)–(c), the measured transmission and reflection results are shown for a normal incidence, with comparison to simulation. The simulation has been adjusted to account for differences in the fabricated device compared to the design, including the larger layer pitch, wider VO_2 area, wider NiCr traces, and the lack of bridges and VO_2 for one set of meanderlines. These changes are summarized in Fig. 14.

The measurement and simulation results have similar trends overall. The measured transmission magnitudes are lower than the simulation, and the difference in phase is closer to 90°. The discrepancies with the simulation can be attributed to angular misalignment of the layers in the fabricated device as well as beam truncation effects. If the layers are not parallel, the mutual coupling between them will be stronger in some areas of the array than others. Additionally, edge diffraction from beam truncation differs between the *thru* calibration standard and the device measurement due to the presence of additional silicon and PCB layers. These nonidealities are not captured in the Floquet port simulations.

TABLE II
COMPARISON OF RECONFIGURABLE LCP CONVERTER METASURFACES FROM THE LITERATURE

Study	Device Operation	LCP AR Bandwidth (GHz)	Axial Ratio (dB)	Loss in-Band (dB)	Reconfiguration method
[4]	Reflection	11.8–24.1 [LHCP]	≤3.0	~1–3	PIN diodes
[5]	Reflection	4.9–8.2 [RHCP]	≤3.0	~1–3	Varactor diodes
[6]	Reflection	8.1–9.7; 9.8–11.2 [RHCP] 8.0–9.7; 9.8–11.1 [LHCP]	≤3.0	N/A	Mechanical
[7]	Transmission	2.49–2.55 [RHCP] 2.47–2.54 [LHCP]	≤3.0	~4	Liquid metal
[8]	Reflection	9.15–11.2 [RHCP] 9.15–11.7 [LHCP]	≤3.0	~1–3	Liquid metal
[9]	Reflection	129.5–130.5 [LHCP & RHCP]	≤6.0	~2.5–4.5	Liquid crystal
[10]	Transmission	2.50–3.64 [RHCP]	≤3.0	~2.5–3 dB	PIN diodes
This Work	**Transmission**	**27.5–31 [LHCP]**	**≤2.1**	**~4**	**Phase-change material**

In Fig. 15(e) and (f), the measured FOM are shown. Measured AR ≤ 2.1 dB in the satcom uplink band, 27.5–31 GHz and AR ≤ 1 dB from a narrower band of 30.2–32.4 GHz. Measured IL ≤ 4.0 dB in the satcom uplink band and IL ≤ 4.06 dB within the 1-dB AR band. It is also worth noting that CP is achieved across the entire measured frequency band, with AR ≤ 2.3 dB from 27–35 GHz (at least 26% CP bandwidth). Measured phase error (φ_e) is between 3.7° and 7.4° in the measured band, while the simulation achieves phase error between 9.7° and 21.3°. As a result, measured AR is lower than simulation, with a minimum of 0.7 dB around 30 GHz. Whereas improvement in losses from simulation to measurement would be considered somewhat unusual, error in phase difference ($\Delta\varphi$) can potentially be positive or negative. Therefore, this fortunate deviation from the simulation is both plausible and reasonable. Measured IL is 1.6–1.9 dB higher than simulation due to the decrease in transmission magnitude for both components.

The increased loss compared to the simulation is mainly attributed to the small size of the test vehicle. In the current setup, truncation of the Gaussian beam and potential angular misalignment of the metasurface layers, which impacts mutual coupling, contributed to the losses. The metasurface active area is 26.4×26.4 mm^2, which is the maximum size that permits fabricating all four layers on a single 100-mm wafer. Fabricating a sufficiently large array to prevent Gaussian beam truncation creates an additional challenge of having four wafers with near-perfect yield. With four layers per wafer, it is possible to account for yield by matching the best chips from multiple wafers. A larger array would have been prohibitively expensive, as many high-yielding wafers would have been required to create a single four-layer device.

Additional loss (about 2 dB) inherent in the design comes as a result of the heaters being connected in both configurations at all times and from the VO$_2$ being less conductive than metal, but future iterations of the design can improve the loss figure. Solutions include increasing inductance of the heaters for improved RF choke in the switch OFF state, which would emphasize the ON state shorting of the metallic heater turns by VO$_2$, as well as improving thermal isolation for the switches, thus decreasing the amount of NiCr needed for sufficient heating current.

Results for incident angle measurements are shown in Fig. 16 with comparison to the simulation. The simulated data show reasonable stability of IL for higher incident angles below 31 GHz, with maximum variation of 0.2 dB. Above 31 GHz, there is a monotonic increase in IL with incident angle, with a maximum increase of 3.1 dB at 40°. The measured IL has less than 0.3 dB variation across the measured band up to 30°, but at 40°, IL is up to 0.5 dB higher compared to normal incidence. For both simulation and measurement, $\Delta\varphi$ decreases for steeper incident angles. As a result, the simulated model's signed φ_e increases by up to 2.8°–11.6° at an incident angle of 40°. Below 32 GHz, this effect leads to a decrease in AR by up to 1.7 dB for higher incident angles. In the upper part of the band, asymmetry in transmission magnitudes dominates, causing an increase in AR by up to 3.9 dB with higher incident angles. On the other hand, the measured data for normal incidence already had $\Delta\varphi$ below 90°. Thus, the decreasing $\Delta\varphi$ results in an increase in φ_e of up to 2.8°–13.0° for an incident angle of 40°. Due to the increasing φ_e, the AR increases up to 0.5–1.8 dB at an incident angle of 40°.

Comparing the measured ON/OFF performance for reconfigurability in Fig. 17, there is stark distinction between the two modes. When cold/deactivated, the metasurface passes LP with IL ≤ 3.08 dB and $\Delta\varphi$ ≤ 1.3°, resulting in AR > 39 dB (AR not shown) in the satcom uplink band. This comparison is shown in Fig. 17. This is in contrast to the LHCP converted wave that exhibits IL ≤ 4.0 dB and AR ≤ 2.1 dB. Thus, we have experimentally confirmed Ka-band LCP conversion using a VO$_2$-based reconfigurable metasurface.

Table II shows a comparison of reconfigurable LCP converters from the literature to illustrate the novelty of our work. We have demonstrated the first example of a transmission-mode reconfigurable LCP converter using VO$_2$ PCM. We also demonstrated ≤2.1 dB of AR across the uplink portion of the Ka band (27.5–31 GHz). Our metasurface targets the mmWave band unlike most other demonstrated designs, and the loss performance is comparable to others despite the higher operating frequency, due to the inherent low loss of PCM-based approaches.

VI. CONCLUSION

In this study, we designed a reconfigurable dual-sense LCP converter metasurface at Ka-band using VO$_2$ as the active material. The dual-sense design was based on two identical

overlapping meanderline unit cells, rotated 90° about an intersection point, where they are isolated in the dc domain and continuous in the RF domain. VO$_2$ was chosen for its simplicity of activation and low material losses at frequencies in the mmWave spectrum, as opposed to semiconductor-based switches. In the design simulation, LHCP and RHCP modes had identical FOM of AR $\leq$ 0.99 dB and IL $\leq$ 2.59 dB in the 27.5–31 GHz uplink band. It was designed and simulated as the first transmission-mode dual-sense LCP conversion metasurface.

Measured results are presented as LP-LHCP conversion, using a device prototype retaining the structures of the RHCP configuration for their effect on RF performance, demonstrating that the only barrier to dual-sense experimental operation is improved thermal isolation. Nevertheless, this device is experimentally validated as the first PCM-based reconfigurable LCP converter and the first reconfigurable LCP conversion metasurface at Ka-band. In the OFF state, the device passes LP waves at IL $\leq$ 3.08 dB and AR $\geq$ 39 dB in the satcom uplink band, and in the ON state, it transmits LHCP waves at IL $\leq$ 4.0 and AR $\leq$ 2.1 dB in the same band. The LHCP transmission mode contains a 1-dB AR band from 30.2–32.4 GHz, where IL $\leq$ 4.1 dB. The increase in IL from simulation to measurement is attributed largely to factors such as beam truncation, diffraction effects from the edges of the device, and the multiple metasurface layers deviating slightly from parallel to each other within the device package. These factors could not be accounted for in infinite-array simulation. The measured LCP conversion performance is stable (ΔAR $\leq$ 1.8 dB) within the target band at incident angles up to 40°, with increase in insertion loss ΔIL $\leq$ 0.5 dB.

ACKNOWLEDGMENT

REFERENCES

[1] M. Del Mastro, M. Ettorre, and A. Grbic, "Dual-band, orthogonally-polarized LP-to-CP converter for SatCom applications," *IEEE Trans. Antennas Propag.*, vol. 68, no. 9, pp. 6764–6776, Sep. 2020, doi: 10.1109/TAP.2020.2989868.

[2] P. Naseri, J. R. Costa, S. A. Matos, C. A. Fernandes, and S. V. Hum, "Equivalent circuit modeling to design a dual-band dual linear-to-circular polarizer surface," *IEEE Trans. Antennas Propag.*, vol. 68, no. 7, pp. 5730–5735, Jul. 2020, doi: 10.1109/TAP.2020.2963949.

[3] F. Greco, E. Arnieri, G. Amendola, L. Boccia, and F. Voci, "Dual band dual circularly polarized antenna with a meanderline polarizer," in *Proc. IEEE Int. Symp. Antennas Propag. USNC/URSI Nat. Radio Sci. Meeting*, Jul. 2018, pp. 119–120, doi: 10.1109/APUS-NCURSINRSM.2018.8608516.

[4] Z. Yang et al., "Reconfigurable multifunction polarization converter integrated with PIN diode," *IEEE Microw. Wireless Compon. Lett.*, vol. 31, no. 6, pp. 557–560, Jun. 2021, doi: 10.1109/LMWC.2021.3064039.

[5] X. Gao, W. L. Yang, H. F. Ma, Q. Cheng, X. H. Yu, and T. J. Cui, "A reconfigurable broadband polarization converter based on an active metasurface," *IEEE Trans. Antennas Propag.*, vol. 66, no. 11, pp. 6086–6095, Nov. 2018, doi: 10.1109/TAP.2018.2866636.

[6] C. Ni, M. S. Chen, Z. X. Zhang, and X. L. Wu, "Design of frequency-and polarization-reconfigurable antenna based on the polarization conversion metasurface," *IEEE Antennas Wireless Propag. Lett.*, vol. 17, pp. 78–81, 2018, doi: 10.1109/LAWP.2017.2775444.

[7] A. H. Naqvi and S. Lim, "Microfluidically polarization-switchable metasurfaced antenna," *IEEE Antennas Wireless Propag. Lett.*, vol. 17, pp. 2255–2259, 2018, doi: 10.1109/LAWP.2018.2872108.

[8] O. M. Sanusi, Y. Wang, and L. Roy, "Reconfigurable polarization converter using liquid metal based metasurface," *IEEE Trans. Antennas Propag.*, vol. 70, no. 4, pp. 2801–2810, Apr. 2022, doi: 10.1109/TAP.2021.3137217.

[9] E. Doumanis et al., "Electronically reconfigurable liquid crystal based mm-wave polarization converter," *IEEE Trans. Antennas Propag.*, vol. 62, no. 4, pp. 2302–2307, Apr. 2014, doi: 10.1109/TAP.2014.2302844.

[10] S. S. Zhu, P. Wang, Y. Zhang, Z. M. Yan, Y. Wang, and H. C. Zhou, "A reconfigurable polarization converter and related application as horn antenna cladding," *J. Appl. Phys.*, vol. 133, no. 2, Jan. 2023, Art. no. 023102, doi: 10.1063/5.0130212.

[11] M. A. Sofi, K. Saurav, and S. K. Koul, "A linear to circular polarization reconfigurable converter based on frequency selective surface," *Microw. Opt. Technol. Lett.*, vol. 63, no. 5, pp. 1425–1433, May 2021, doi: 10.1002/mop.32779.

[12] Z. Yang, C. Ko, and S. Ramanathan, "Oxide electronics utilizing ultrafast metal-insulator transitions," *Annu. Rev. Mater. Res.*, vol. 41, no. 1, pp. 337–367, Aug. 2011, doi: 10.1146/annurev-matsci-062910-100347.

[13] D. West et al., "VO$_2$-based reconfigurable electromagnetic surfaces," presented at the URSI Int. Symp. Electromagn. Thoery (EMTS), Vancouver, BC, Canada, 2023.

[14] D. West, M. Lust, and N. Ghalichechian, "Characterization of VO$_2$-based reconfigurable linear-to-circular polarization converter," presented at the IEEE Int. Symp. Antennas Propag. USNC-URSI Radio Sci. Meeting (USNC-URSI), Portland, OR, USA, Jul. 2023.

[15] S. Chen, M. Lust, and N. Ghalichechian, "Antenna-coupled microbolometer based on VO$_2$'s non-linear properties across the metal–insulator transition region," *Appl. Phys. Lett.*, vol. 121, no. 20, Nov. 2022, Art. no. 201901, doi: 10.1063/5.0123779.

[16] S. Chen, M. Lust, and N. Ghalichechian, "Multiphysics simulation of hypersensitive microbolometer sensor using vanadium dioxide and air suspension for millimeter wave imaging," *Microsyst. Technol.*, vol. 27, no. 7, pp. 2815–2822, Jul. 2021, doi: 10.1007/s00542-020-05031-0.

[17] K. Maeda, V. N. Hai, K. Nishioka, A. Matsutani, T. Tachiki, and T. Uchida, "Evaluation of characteristics in VO$_x$ microbolometer fabricated by MOD on Si$_3$N$_4$/SiO$_2$ membrane," *Electron. Commun. Jpn.*, vol. 102, no. 3, pp. 12–20, Mar. 2019, doi: 10.1002/ecj.12150.

[18] C. Chen, X. Yi, X. Zhao, and B. Xiong, "Characterizations of VO$_2$-based uncooled microbolometer linear array," *Sens. Actuators A, Phys.*, vol. 90, no. 3, pp. 212–214, May 2001, doi: 10.1016/s0924-4247(01)00495-2.

[19] D. E. Anagnostou, D. Torres, T. S. Teeslink, and N. Sepulveda, "Vanadium dioxide for reconfigurable antennas and microwave devices: Enabling RF reconfigurability through smart materials," *IEEE Antennas Propag. Mag.*, vol. 62, no. 3, pp. 58–73, Jun. 2020, doi: 10.1109/MAP.2020.2964521.

[20] Z. Li, X. Wu, Z. Wu, Y. Jiang, J. Xu, and Z. Liu, "Tunable mid-infrared patch antennas based on VO$_2$ phase transition," *J. Modern Opt.*, vol. 64, no. 17, pp. 1762–1767, Sep. 2017, doi: 10.1080/09500340.2017.1314030.

[21] W. Vitale et al., "Steep slope VO$_2$ switches for wide-band (DC-40 GHz) reconfigurable electronics," in *Proc. 72nd Device Res. Conf.*, 2014, pp. 29–30.

[22] A. Crunteanu et al., "Voltage- and current-activated metal–insulator transition in VO$_2$-based electrical switches: A lifetime operation analysis," *Sci. Technol. Adv. Mater.*, vol. 11, no. 6, Dec. 2010, Art. no. 065002, doi: 10.1088/1468-6996/11/6/065002.

[23] N. El-Hinnawy et al., "A four-terminal, inline, chalcogenide phase-change RF switch using an independent resistive heater for thermal actuation," *IEEE Electron Device Lett.*, vol. 34, no. 10, pp. 1313–1315, Oct. 2013, doi: 10.1109/LED.2013.2278816.

[24] C. Hillman, P. A. Stupar, J. B. Hacker, Z. Griffith, M. Field, and M. Rodwell, "An ultra-low loss millimeter-wave solid state switch technology based on the metal-insulator-transition of vanadium dioxide," in *IEEE MTT-S Int. Microw. Symp. Dig.*, Sep. 2014. [Online]. Available: https://www.scopus.com/inward/record.uri?eid=2-s2.0-84905011543&doi=10.1109%2fMWSYM.2014.6848479&partnerID=40&md5=4ceb42 0161fff0873723d9920d62cf9d, doi: 10.1109/MWSYM.2014.6848479.

[25] T. Singh and R. R. Mansour, "Loss compensated PCM GeTe-based latching wideband 3-bit switched true-time-delay phase shifters for mmWave phased arrays," *IEEE Trans. Microw. Theory Techn.*, vol. 68, no. 9, pp. 3745–3755, Sep. 2020, doi: 10.1109/TMTT.2020.3007833.

[26] J. Lee et al., "Epitaxial VO$_2$ thin film-based radio-frequency switches with thermal activation," *Appl. Phys. Lett.*, vol. 111, no. 6, Aug. 2017, Art. no. 063110, doi: 10.1063/1.4998452.

[27] M. R. M. Hashemi, S.-H. Yang, T. Wang, N. Sepúlveda, and M. Jarrahi, "Electronically-controlled beam-steering through vanadium dioxide metasurfaces," *Sci. Rep.*, vol. 6, no. 1, p. 35439, Oct. 2016, doi: 10.1038/srep35439.

[28] V. Sanphuang, N. Ghalichechian, N. K. Nahar, and J. L. Volakis, "Reconfigurable THz filters using phase-change material and integrated heater," *IEEE Trans. THz Sci. Technol.*, vol. 6, no. 4, pp. 583–591, Jul. 2016, doi: 10.1109/TTHZ.2016.2560175.

[29] A. Sarangan, J. Duran, V. Vasilyev, N. Limberopoulos, I. Vitebskiy, and I. Anisimov, "Broadband reflective optical limiter using GST phase change material," *IEEE Photon. J.*, vol. 10, no. 2, pp. 1–9, Apr. 2018, doi: 10.1109/JPHOT.2018.2796448.

[30] P. O. Leisher et al., "Photonic limiters with enhanced dynamic range," presented at the 4th Compon. Packag. Laser Syst., 2018.

[31] N. Antonellis, R. Thomas, M. A. Kats, I. Vitebskiy, and T. Kottos, "Nonreciprocity in photonic structures with phase-change components," *Phys. Rev. Appl.*, vol. 11, no. 2, Feb. 2019, Art. no. 024046, doi: 10.1103/physrevapplied.11.024046.

[32] M. Lust, S. Chen, C. E. Wilson, J. Argo, V. Doan-Nguyen, and N. Ghalichechian, "High-contrast, highly textured VO$_2$ thin films integrated on silicon substrates using annealed Al$_2$O$_3$ buffer layers," *J. Appl. Phys.*, vol. 127, no. 20, 2020, Art. no. 205303, doi: 10.1063/1.5144816.

[33] S. Chen, M. Lust, A. Roo, and N. Ghalichechian, "Reliability of VO$_2$-based mmWave switches under 100 million thermal cycles," *IEEE Trans. Device Mater. Rel.*, vol. 23, no. 2, pp. 241–248, Feb. 2023, doi: 10.1109/TDMR.2023.3249771.

[34] M. Lust, I. Vitebskiy, I. Anisimov, and N. Ghalichechian, "Thermo-optic VO$_2$-based silicon waveguide mid-infrared router with asymmetric activation thresholds and large bi-stability," *Opt. Exp.*, vol. 31, no. 14, p. 23260, 2023, doi: 10.1364/oe.493895.

[35] B. Munk, *Frequency Selective Surfaces*. Hoboken, NJ, USA: Wiley, 2000.

[36] M.-A. Joyal and J.-J. Laurin, "Analysis and design of thin circular polarizers based on meander lines," *IEEE Trans. Antennas Propag.*, vol. 60, no. 6, pp. 3007–3011, Jun. 2012, doi: 10.1109/TAP.2012.2194659.

[37] M. Lust and N. Ghalichechian, "VO2-based reconfigurable meanderline polarizer at Ka-band," in *Proc. IEEE Int. Symp. Antennas Propag. USNC-URSI Radio Sci. Meeting (APS/URSI)*, Dec. 2021, pp. 551–552.

[38] B. Ghassemiparvin and N. Ghalichechian, "Reconfigurable antennas: Quantifying payoffs for pattern, frequency, and polarisation reconfiguration," *IET Microw., Antennas Propag.*, vol. 14, no. 3, pp. 149–153, Feb. 2020.

[39] P. F. Goldsmith, *Quasioptical Systems: Gaussian Beam Quasioptical Propagation and Applications*. Piscataway, NJ, USA: IEEE Press, 1998.

David L. West (Graduate Student Member, IEEE) received the B.S.E. degree (summa cum laude) in electrical engineering from the University of South Carolina, Columbia, SC, USA, in 2022. He is currently pursuing the Ph.D. degree in electrical engineering with Georgia Institute of Technology, Atlanta, GA, USA.

His research interests include antenna arrays, metasurfaces, vanadium dioxide phase change material, and wireless power transfer.

Mr. West has served as a reviewer for IEEE TRANSACTIONS ON ANTENNAS AND PROPAGATION and IEEE ANTENNAS AND WIRELESS PROPAGATION LETTERS, since 2022. He was awarded the IEEE Microwave Theory and Techniques Society Undergraduate Scholarship in 2020, and received the Georgia Tech President's Fellowship in 2022.

Vanessa Smet, photograph and biography not available at the time of publication.

Thomas G. Williamson (Member, IEEE) received the B.S.E.E. (summa cum laude) and M.S.E.E. degrees from North Carolina State University, Raleigh, NC, USA, in 2018 and 2019, respectively. He is currently pursuing the Ph.D. degree with Georgia Institute of Technology, Atlanta, GA, USA.

Currently, he is a Research Engineer at Georgia Tech Research Institute (GTRI), Atlanta. He works in the Antenna Systems Division of the Sensors and Electromagnetic Applications Laboratory. He is a member of the mmWave Antennas and Arrays Laboratory, Georgia Institute of Technology. His research areas include radar systems, antennas, arrays, filters, RFICs, phase change materials, power amplifiers, low noise amplifiers, other RF frontend electronics, digital arrays, and digital array radars. He is a U.S. Marine Corps veteran. During his service (2009–2014), he completed three deployments, attained the rank of Sergeant, and held multiple small unit leadership roles. He has led multiple internal research and development projects and sponsored projects at GTRI.

Mr. Williamson received various commendations for excellence and meritorious service, including the Navy Achievement Medal. He received the Dean's Fellowship award at NC State University in 2018. He won the Department of Defense National Defense Science and Engineering Graduate Fellowship (NDSEG) in 2019, which he declined to work at GTRI. He received the GTRI Star Performer Award in 2021.

Mark S. Lust (Student Member, IEEE) received the B.S. (cum laude), M.S., and Ph.D. degrees in electrical and computer engineering from The Ohio State University, Columbus, OH, USA, in 2018, 2022, and 2023, respectively.

There, he worked at the ElectroScience Laboratory and Nanotech West Laboratory, and his research studies included antennas, phase change materials, microfabrication, frequency selective surfaces/metasurfaces, on-chip RF measurement, multiphysics simulation, and integrated optics. His research began during his undergraduate studies in the RF Microsystems group, continuing into graduate school, and for his last year of Ph.D. studies was associated with the mmWave Antennas and Arrays Laboratory, Georgia Institute of Technology, Atlanta, GA, USA, while remaining at The Ohio State University. Currently, he is working at Battelle Memorial Institute in the Cyber Trust and Analytics division.

Dr. Lust won The Ohio State University Fellowship Award entering his doctoral studies in 2018, followed by the Defense Associated Graduate Student Innovators (DAGSI) Fellowship in 2019.

Nima Ghalichechian (Senior Member, IEEE) received the B.S. degree in electrical engineering from Amirkabir University of Technology, Tehran, Iran, in 2001, and the M.S. and Ph.D. degrees in electrical engineering from University of Maryland, College Park, MD, USA, in 2005 and 2007, respectively.

He is an Assistant Professor at the School of Electrical and Computer Engineering, Georgia Institute of Technology, Atlanta, GA, USA. His research area is in electromagnetics, specifically, mmWave phased arrays, reflectarrays, transmitarrays, meta-surfaces, on-chip antennas, ultra-wideband antennas, novel reconfiguration techniques, phase-change materials, 3-D-printed lenses and arrays, and robotic measurements of antennas. He held a Research Scientist and a Research Assistant Professor positions at OSU from 2012 to 2017. From 2007 to 2012, he was with the Research Department of FormFactor Inc., Livermore, CA, USA, as a Senior Principal Engineer.

Prof. Ghalichechian is the Director of the mmWave Antennas and Arrays Laboratory, Georgia Tech. He is currently an Associate Director of Georgia Electronic Design Center (GEDC) and an Associate Editor of the IEEE TRANSACTIONS ON ANTENNAS AND PROPAGATION. He was an Associate Editor of the IEEE ANTENNAS AND WIRELESS PROPAGATION LETTERS from 2019 to 2022. Prior to joining Georgia Tech in 2021, he was an Assistant Professor at The Ohio State University (OSU), Columbus, from 2017 to 2021. He is a recipient of the 2018 College of Engineering Lumley Research Award at OSU, 2019 NSF CAREER Award, 2019 U.S. Air Force Faculty Summer Fellowship Award, and 2020 ECE Excellence in Teaching Award at OSU.